Complementary methods for cluster size distribution measurements: supported platinum nanoclusters in methane reforming catalysts

J.M. Ramallo-López[a], F.G. Requejo[a,*], A.F. Craievich[b], J. Wei[c], M. Avalos-Borja[d], E. Iglesia[c]

[a] *Departamento de Física and IFLP, FCE, Universidad Nacional de La Plata, CC/67, 1900 La Plata, BA, Argentina*
[b] *Institute of Physics, University of Sao Paulo, CEP 05508-900 Sao Paulo, SP, Brazil*
[c] *Department of Chemical Engineering, University of California at Berkeley, Berkeley, CA 94720, USA*
[d] *Centro de Ciencias de la Materia Condensada, UNAM, A. Postal 2681, Ensenada, BC 22800, Mexico*

Available online 11 November 2004

Abstract

Pt cluster size strongly influences the reactivity of surfaces for C−H bond activation during CH_4 steam reforming. C−H bond activation turnover rates for H_2O reforming of CH_4 increased with decreasing Pt cluster size, suggesting that coordinatively unsaturated surface Pt atoms are more reactive than Pt atoms in low-index surfaces prevalent in larger clusters. Near-edge fine structure in X-ray absorption spectra clearly shows electronic changes in Pt clusters relative to bulk Pt crystallites, though differences in the 5d electronic density among samples with different cluster size could not be related directly to Pt surface atom coordination. These results suggest that catalytic consequences of cluster size arise from surface structure changes leading to coordinative unsaturation of surface atoms. X-ray absorption and small angle X-ray scattering techniques were used to measure the size of Pt metal nanoclusters and the results are compared with H_2 chemisorption and transmission electron microscopy data.
© 2004 Elsevier B.V. All rights reserved.

Keywords: Cluster size; SAXS; XAFS; HRTEM; Methane reforming

1. Introduction

Supported metal clusters are widely used to catalyze chemical reactions, such as methanation [1,2], reforming [3–5], and partial oxidation [6]. The size of these clusters strongly influence the turnover rates and selectivities for structure-sensitive catalytic reactions [7]. For CO_2–CH_4 and H_2O–CH_4 reforming and CH_4 decomposition reactions, CH_4 activation turnover rates increased with decreasing size of Rh [8], Ru [9], Ir [10] and Pt [11] clusters, consistent with experimental and theoretical evidence for the higher reactivity of coordinatively unsaturated surface atoms on single crystals [12–14]. Pt surfaces show higher reactivity for the activation of C−H bonds in CH_4 than the other noble metals (Rh, Ru, Ir) for a given cluster size [11]. Typical methods for measuring the number of

metal atoms exposed at cluster surfaces rely on their titration by chemisorbed hydrogen or CO or on structural assessment by transmission electron microscopy. These methods provide critical details, but when coordination and electronic properties of surface atoms are most relevant for their catalytic properties, they must be complemented by spectroscopic assessments that provide these essential details.

Other experimental methods can be used to probe the size of metal clusters dispersed in a porous substrate. Small-angle X-rays scattering (SAXS) is particularly sensitive to the size and shape of nanometric clusters, while the results are essentially independent of the detailed atomic structure of these clusters. The level of detail available from SAXS data depends on the structural complexity of the system, and the accuracy of the size estimates is greatest for random distributions of clusters of uniform size and shape [15,16]. In contrast, local structure can be probed at the atomic level using EXAFS, which also provides information about cluster size from

average coordination numbers, which depend sensitively on size for clusters of nanometric diameter.

Here, we compare and discuss the EXAFS, SAXS, high-resolution transmission electron microscopy (HRTEM) and chemisorption techniques to determine Pt cluster size in Pt-based supported catalysts useful in the synthesis of H_2/CO mixtures from CH_4–H_2O and CH_4–CO_2 reactant mixtures.

2. Experimental

Pt/Al_2O_3, Pt/ZrO_2 and Pt/ZrO_2–CeO_2 with varying Pt content (0.2–1.6 wt.%) were prepared by incipient wetness impregnation of Al_2O_3, ZrO_2 and ZrO_2–CeO_2 with aqueous $H_2PtCl_6 \cdot 6H_2O$ solutions (Aldrich, Lot# 10013LO, 99%) and their catalytic behavior is reported here. Samples were dried in ambient air at 393 K and then treated in flowing dry air (Airgas, UHP, 1.2 cm^3/g s) at 873 K (0.167 K s^{-1}) for 5 h. Samples were reduced in H_2 (Airgas, UHP, 50 cm^3/g s) at 873 K (0.167 K s^{-1}) for 2 h before reforming reactions. Al_2O_3, ZrO_2 and ZrO_2–CeO_2 (Zr/Ce = 4) was prepared as previously described [11].

2.1. H_2 Chemisorption

The fraction of the Pt atoms exposed at cluster surfaces, denoted here as the Pt dispersion, was estimated from H_2 chemisorption uptakes measured at 373 K using a Quantasorb chemisorption analyzer (Quantachrome Corp.). Catalysts were treated in H_2 at 873 K for 2 h, then evacuated at 10^{-6} Torr for 0.5 h at 873 K. Samples were cooled in vacuum to 373 K and a H_2 chemisorption isotherm was measured between 3 and 50 kPa. A backsorption isotherm was measured by repeating this procedure after evacuating the sample at 373 K for 0.5 h. The difference of the two isotherms provides the strongly chemisorbed hydrogen uptakes. Pt dispersions were calculated by assuming that one hydrogen atom chemisorbed on each surface Pt. These dispersions were also used to estimate average crystallite diameters by assuming hemispherical geometry using:

$$D = \frac{1}{d} \tag{1}$$

where D is the fractional dispersion and d is the crystallite diameter (nm) [17].

2.2. Catalytic reactions of methane

H_2O–CH_4 reforming reaction rates were measured at 873 K using samples (5 mg) held within a quartz tube [11]. Reactants consisted of 50% CH_4/Ar (Matheson; certified mixtures) diluted with He (Airgas, UHP). H_2O was introduced by syringe pump and all transfer lines were kept above 373 K. Effluent streams were analyzed by gas chromatography using thermal conductivity detection. Measured CH_4 reaction rates were converted to forward re-

action rates using approach to equilibrium formalisms [11].

2.3. High-resolution transmission electron microscopy (TEM)

High-resolution transmission electron micrographs of fresh samples were obtained with JEOL 2010 and JEOL 2010-F electron microscopes with point-to-point resolution greater than 0.19 nm. Samples were crushed in an agate mortar, suspended in isopropanol, and a drop of the resulting slurry was placed on a holey carbon copper grid and dried in ambient air. Micrographs were recorded predominately in sample regions that avoided interference with the carbon support. Pt crystallite size distributions were obtained by manual measurements of enlarged prints made from digitized negatives by counting at least 200 crystallites.

2.4. Small-angle X-ray scattering (SAXS)

Small-angle X-ray scattering (SAXS) measurements were performed at the Synchrotron Light National Laboratory (LNLS) in Campinas, Brazil, using D11 SAS beam-line. The setup is equipped with a silicon(1 1 1) monochromator giving a horizontally focused X-ray beam with $\lambda = 1.61$ Å [18]. The scattering intensity curves were measured using a gas 1D position-sensitive X-ray detector (Biologic) as a function of the modulus of the scattering vector [$q = (4\pi/\lambda) \sin(\varepsilon/2)$], ε being the scattering angle. Parasitic scattering from collimation slits was subtracted from the measured signal. Mathematical desmearing of experimental intensities was not required because of the narrow detector slit and the small incident beam cross-section at the detection plane.

SAXS results were analyzed using Porod [15] and Guinier [16] equations. Porod equation describes the asymptotic scattering intensity, at high q, produced by two-phase materials whose electron density can be well described by a two-density model. It is given by [15]

$$I(q) = 2\pi(\rho_1 - \rho_2)^2 \frac{S}{q^4} \tag{2}$$

where ρ_1 and ρ_2 are the electron densities of each phase and S the interface surface area between the two phases. Typical deviations from the asymptotic function $I(q)$ from Eq. (2) reflect an additive and constant contribution to the scattering intensity from statistical density fluctuations and/or very small structure defects in the matrix [19]. Guinier equation describes the X-ray scattering intensity for small q values, corresponding to dilute systems of isolated and nano-objects. For a two electron density system composed of identical and homogeneous nanometric objects embedded in a homogeneous matrix, the scattering intensity $I(q)$ is given by [16]

$$I(q) = N(\rho_1 - \rho_2)^2 v^2 e^{-(1/3)R_g^2 q^2} \tag{3}$$

where N is the number of objects per unit volume and v and R_g their volume and radius of gyration, respectively. For an spherical object of radius R, we have $R = \sqrt{5/3}R_g$, and thus the exponent in Eq. (3) becomes equal to $-R^2 q^2/5$.

2.5. X-ray absorption (XANES and EXAFS)

X-ray absorption spectra were measured in the XAS beamline at the National Synchrotron Light Laboratory (LNLS), Campinas, Brazil. EXAFS spectra at the Pt L_3 (11.6 keV) and L_2 (13.3 keV) edges were acquired in transmission mode at ambient temperature using a Si(1 1 1) crystal monochromators in the 11,460–12,600 eV energy range. Samples were sealed in Ar after reduction in H_2 using a sample holder with Kapton walls to avoid contact with ambient air and oxidation of Pt cluster.

XAFS data were extracted from measured spectra using standard methods [20,21]. Six individual spectra were averaged and the pre-edge region fitted to a second order polynomial curve and post-edge background was subtracted using cubic spline routines after spectra were normalized by the absorption edge height. The fine structure region was analyzed using Fourier transform methods. Phase shifts and amplitude functions for Pt–Pt pairs were obtained from FEFF7 [22] codes using a cluster of metallic Pt (fcc structure).

At the Pt L_3-edge, allowed bound-state to bound-state transitions from $2p_{3/2}$ to vacant 5d-states in absorbing atom give rise to a resonance peak (white line) above the edge. The line shape of the resonance contains information on the type of final state involved in the transition. Lytle et al. [23] have shown that increases in the resonance peak intensity with respect to the pure element reflect the number of d-electrons removed from the absorber during formation of chemical bonds. Lytle [24] showed that the L_3 resonance peak areas for third-row transition metals increased from Au to Ta, concurrently with the expected increase in the number of vacancies in the d band. Meitzner et al. [25] found similar trends for Re, Os, Ir, Pt and Au and also observed that the resonance feature was more intense for highly dispersed clusters than for the bulk metal. A modified version of the method described by Mansour et al. [26] and Reifsnyder [27] was used to quantify differences in white line intensity between catalysts and the Pt foil. After subtracting the Pt foil data from the Pt cluster data, the resulting curves were integrated between -10 and $+14$ eV at both the L_2 (ΔA_2) and L_3 (ΔA_3) edges. The fractional change in the total number of d-band vacancies in each sample relative to the Pt foil (f_d) was calculated using:

$$f_d = \frac{\Delta A_3 \sigma_3 + 1.11 \Delta A_2 \sigma_2}{A_{3r}\sigma_3 + 1.11 A_{2r}\sigma_2} \tag{4}$$

The areas are normalized [28] by multiplying by the X-ray absorption cross section at the edge jump (σ). Values of 117.1 and 54.2 $cm^2 g^{-1}$ were used for the absorption cross section at the Pt L_3 and L_2 edges [29], respectively.
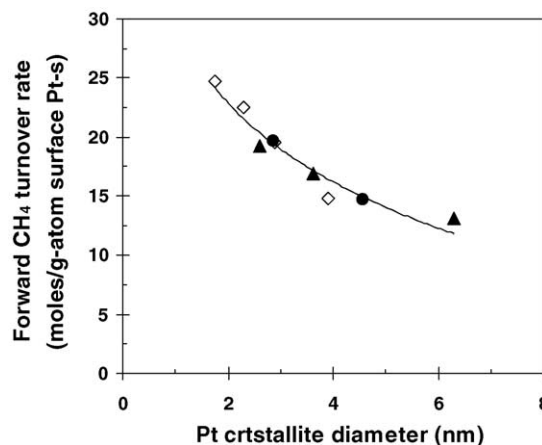

Fig. 1. Forward CH_4 reforming turnover rates using H_2O–CH_4 reactants as a function of Pt dispersion on various supports (873 K, 20 kPa CH_4, (▲) Pt/ZrO$_2$, (●) Pt/γ-Al$_2$O$_3$, (◇) Pt/ZrO$_2$–CeO$_2$).

3. Results and discussion

3.1. Methane activation and chemical conversion on Pt clusters

The activation of methane is a crucial step in many catalytic processes that involve direct conversion of methane to other chemicals. Extensive studies of methane dissociation on various forms of metal surfaces crystals have been carried out, as describe in a review by Pitchai and Klier [30]. Methane activation studies on model surfaces have concluded that activation of C−H bonds depends sensitively on surface structure; specifically, surface steps and kinks are much more active than atoms on close-packed surfaces [31–33].

The effects of Pt cluster size on CH_4 turnover rates for CH_4–H_2O reaction are shown in Fig. 1. The dispersions measured by H_2 chemisorption on fresh catalysts were used to calculate the CH_4 turnover rates and the Pt crystallite diameter. Forward CH_4 reforming turnover rates, which were normalized by the number of exposed Pt atoms and calculated from net rates by correcting for their approach to equilibrium, increased monotonically with decreasing Pt clusters or increasing dispersion. Surface roughness and coordinative unsaturation increase as metal clusters become smaller, suggesting that coordinatively unsaturated Pt surface atoms, prevalent in small crystallites, are indeed more active than atoms on the low-index surfaces predominantly exposed on larger crystallites for the kinetically relevant C−H bond activation step involved in these reactions.

3.2. Transmission electron microscopy

Figs. 2 and 3 show the images and size distributions for the fresh 0.8 and 1.6 wt.% Pt/Al$_2$O$_3$ samples, respectively. The
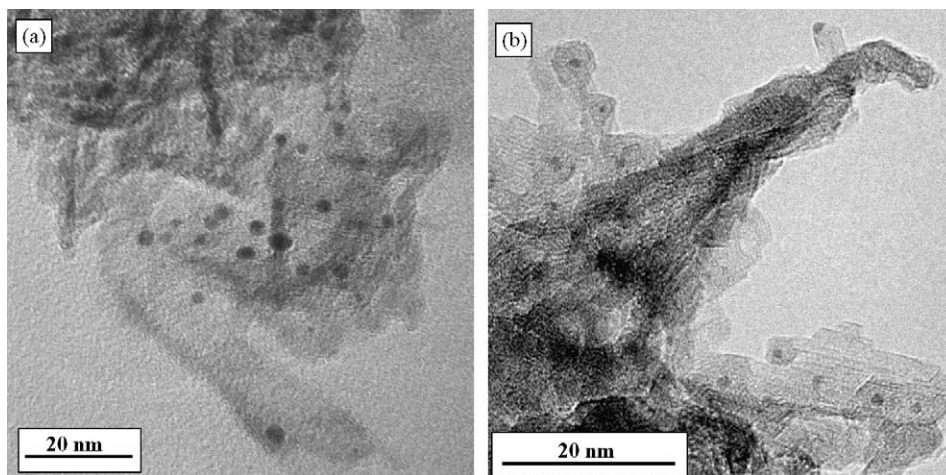
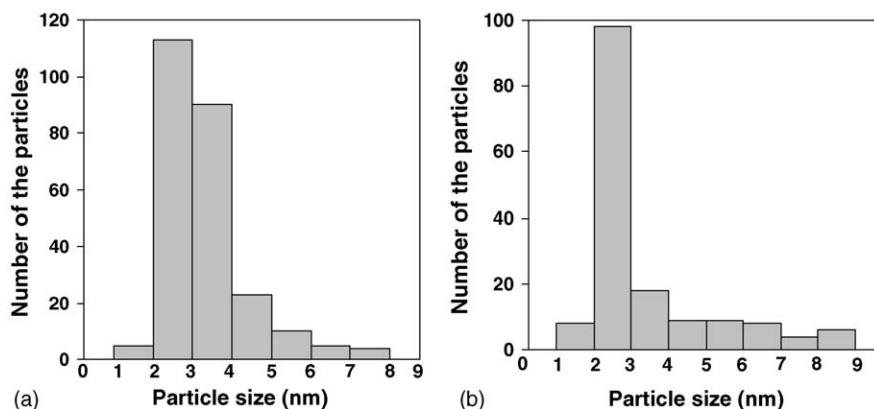Fig. 2. TEM images of (a) 0.8 wt.% Pt/Al_2O_3 and (b) 1.6 wt.% Pt/Al_2O_3 catalysts.

Fig. 3. Crystallite diameter distributions for fresh catalysts (a) 0.8 wt.% Pt/Al_2O_3 and (b) 1.6 wt.% Pt/Al_2O_3 measured by transmission electron microscopy (the error in size distribution is about 10%).

surface-averaged Pt cluster diameters, calculated from [34]

$$\mathrm{d}s = \frac{\sum n_i d_i^3}{\sum n_i d_i^2} \qquad (5)$$

were 2.8 and 4.9 nm for 0.8 and 1.6 wt.% Pt/Al_2O_3, respectively. Pt fractional dispersions measured from H_2 chemisorption were 0.35 and 0.22 for these two samples. These chemisorption uptakes and the assumption of hemispherical-shaped clusters lead to average cluster diameters of 2.9 and 4.5 nm for 0.8 and 1.6 wt.% Pt/Al_2O_3 samples, respectively, in agreement with transmission electron microscopy measurements.

3.3. Small-angle X-ray scattering

Fig. 4 displays the small-angle scattering intensity curves in double-logarithmic scale for a pure porous alumina substrate (a) and for the same substrate containing Pt clusters (b and c). The scattering intensity from the pure porous substrate displays a nearly linear behavior with a slope α of -4, indicating that the Porod equation (Eq. (2)) is applicable over
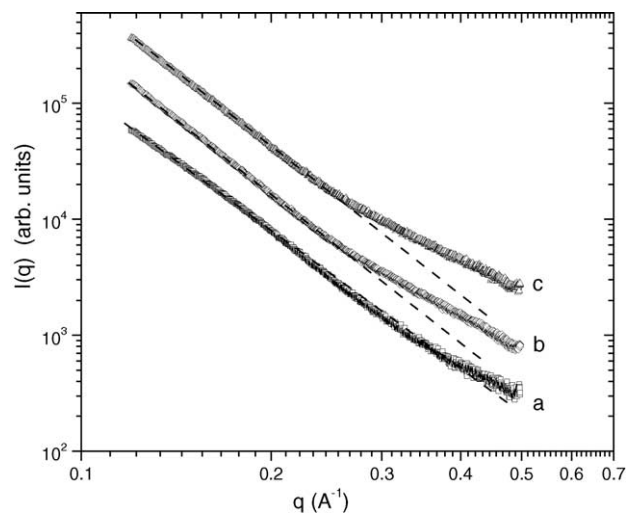

Fig. 4. Small-angle scattering intensity curves in log–log scale corresponding to (a) alumina substrate and to the same substrate containing Pt clusters: (b) with 0.8 wt.% Pt and (c) with 1.6 wt.% Pt before catalytic reaction.

a wide range of q values in these samples. This indicates, in turn, that the two electron density model is accurate for porous alumina. These data also indicate that the pores are relatively large because only the asymptotic part, at high q, of the scattering curve is described accurately by the Porod equation (Eq. (2)). A slight and positive deviation from Porod equation observed at high q ($q > 0.4 \, \text{Å}^{-1}$) reflects a weak and constant contribution from electron density fluctuations in the alumina matrix [16].

The scattering curves associated to the porous substrates containing Pt clusters (Fig. 4b and c) exhibit linear behavior in the $0.12 \, \text{Å}^{-1} < q < 0.20 \, \text{Å}^{-1}$ range and the slope is greater in magnitude than for the pure alumina support. The curves corresponding to the three data sets (a, b and c) become nearly parallel (with a slope $\alpha = -4$), as expected from the Porod equation (dashed lines), in the central region of the scattering curves ($0.2 \, \text{Å}^{-1} < q < 0.3 \, \text{Å}^{-1}$). This q^{-4} dependence of the scattering intensity reflects the scattering produced by the pores. In contrast, the scattering curves corresponding to samples containing Pt clusters exhibit a clear deviation from this q^{-4} behavior at high q ($q > 0.3 \, \text{Å}^{-1}$), which was assigned to scattering by Pt nanoclusters. This effect is predominant at high q values, for which the q^{-4} contribution from pores becomes very small.

A precise and rigorous assessment of the contribution from Pt clusters to the total SAXS intensity – produced by clusters and pores – is generally difficult because this systems consists of a matrix with two types of embedded nanometer-sized objects; thus the simple two-electron density model does not apply. Instead of using complex SAXS data treatment procedures based on a three electron density model [35], we have assumed that the scattering intensity from Pt clusters can be derived by subtracting the scattering intensity produced by pure alumina samples from the total scattering intensity curves. From basic scattering theory, we conclude that scattering by pores and Pt nanoclusters are additive as long as the two types of scattering objects are spatially uncorrelated [16]. In the system studied here, the differences in electron density between Pt clusters and their surroundings are much greater than the corresponding difference for pores and, on the other hand, the clusters are much smaller than the pores. This makes the Pt cluster contributions to the scattering intensity clearly dominant for high q values (for $q > 0.3 \, \text{Å}^{-1}$). Then, even if pores and Pt clusters exhibit some spatial correlation, the subtraction procedure can still be applied in our case as a reasonable approximation. An alternate and more precise analysis of the scattering intensities from Pt nanoclusters embedded in porous matrix can be performed using anomalous small-angle X-ray scattering methods (ASAXS) [36].

SAXS data were analyzed to estimate an average cluster radius, as well as the qualitative features of the size distribution in these samples. We have assumed as a first approximation that the clusters are spherical. In order to estimate the scattering contribution from Pt clusters, we subtracted the scattering intensity from pure alumina from the total scattering curves for each catalyst. Since these materials are in
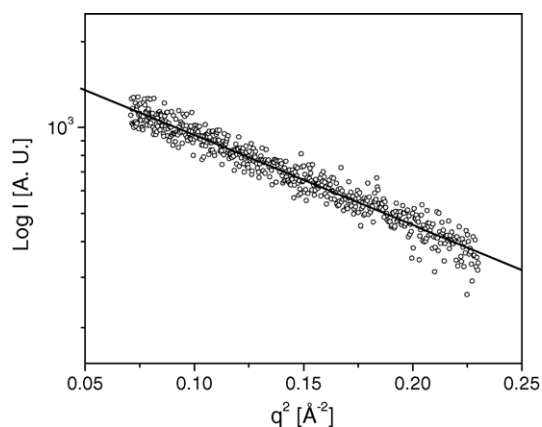

Fig. 5. Guinier plot of SAXS results for Pt clusters in sample 0.8 wt.% Pt/Al_2O_3 after reduction in H_2 at 873 K for 2 h and linear fit yielding a slope $\alpha = -3.1 \, \text{Å}^2$.

powder form, the scale factors for each SAXS curve are not accurately known. Thus, we have estimated them by using values for which the difference curves become well described by the Guinier equation (Eq. (3)) over the q range where Pt cluster contributions are dominant. Guinier plots (log $i(q)$ versus q^2) of these difference curves are shown in Figs. 5 and 6. Their linear behavior over a wide q range indicates that Pt clusters have a relatively narrow size distribution. The cluster radii, obtained from the slopes of the data in Figs. 5 and 6, are 0.60 ± 0.04 and 0.72 ± 0.03 nm for Pt(0.8 wt.%)/Al_2O_3 and Pt(1.6 wt.%)/Al_2O_3, respectively, corresponding to diameters of 1.20 and 1.44 nm.

Our SAXS results indicate the presence of nanoclusters with 1.2–1.44 nm in diameter, but do not detect larger clusters apparent in electron micrographs of the same samples. These large clusters approach the size of the alumina pores and their contributions to SAXS intensity concentrates over the small q range ($q < 0.3 \, \text{Å}^{-1}$), where the contribution from porosity is dominant. Notice that we have applied the substraction procedure over the range of q values above $0.3 \, \text{Å}^{-1}$,
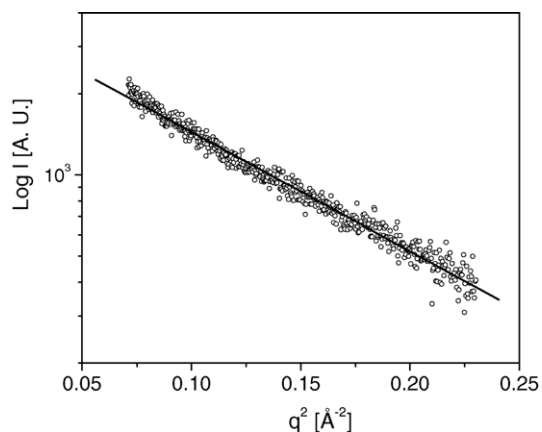

Fig. 6. Guinier plot of SAXS results for Pt clusters in sample 1.6 wt.% Pt/Al_2O_3 after reduction in H_2 at 873 K for 2 h and linear fit yielding a slope $\alpha = -4.4 \, \text{Å}^2$.
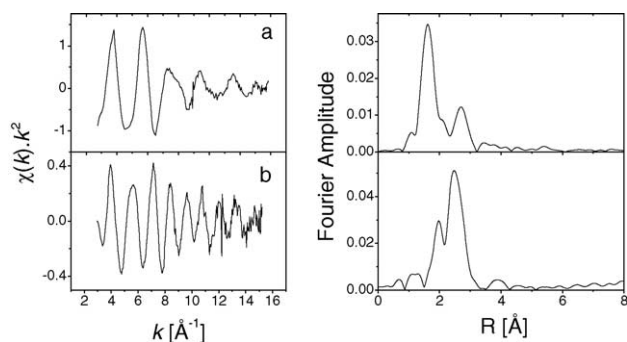
Fig. 7. EXAFS oscillation (left) and their corresponding Fourier transforms (right) of 0.8 wt.% Pt/Al$_2$O$_3$ samples after calcination in flowing dry air at 873 K for 5 h (a) and after reduction in H$_2$ at 873 K for 2 h measured in situ (b).
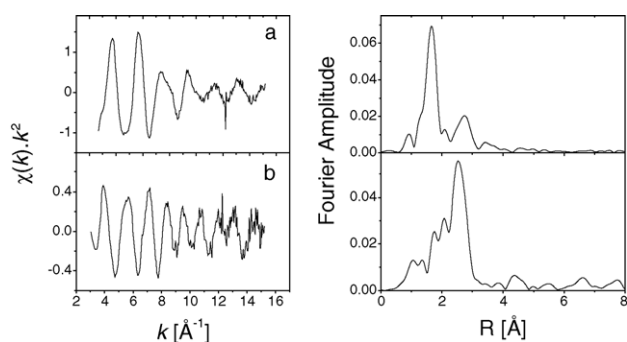

Fig. 8. EXAFS oscillation (left) and their corresponding Fourier transforms (right) of 1.6 wt.% Pt/Al$_2$O$_3$ samples after calcination in flowing dry air at 873 K for 5 h (a) and after reduction in H$_2$ at 873 K for 2 h measured in situ (b).

where the contribution to the scattering from pores can be safely neglected. Thus, for $q \geq 0.3 \, \text{Å}^{-1}$ SAXS detects rather small clusters ($R \sim 1$ nm) thus providing a useful complement to electron microscopy, which detects clusters smaller than 1 nm with some difficulty. As a result, SAXS and HRTEM provide complementary information about the size of Pt clusters, revealing the presence of very small Pt clusters together with larger ones. These arguments indicate that scattering data treatment applying Guinier equation (Eq. (3)) underestimates the actual average radius of Pt clusters.
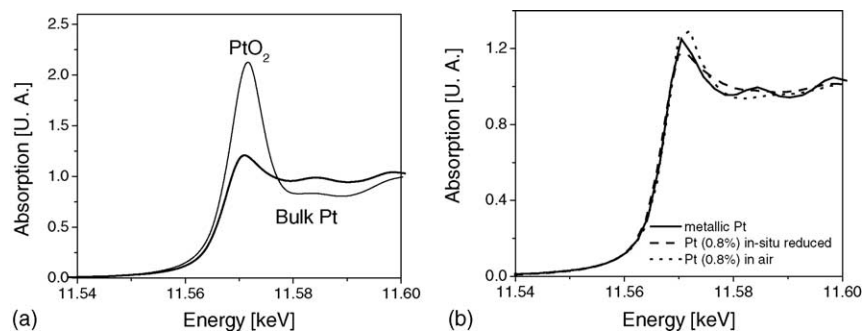
Table 1
EXAFS fitted results for Pt–Pt coordination shell. The errors in the last digit are shown between parenthesis

Sample	Coordination number	Pt–Pt distance (Å)
0.8 wt.% Pt/Al$_2$O$_3$	7.5 (9)	2.67 (1)
1.6 wt.% Pt/Al$_2$O$_3$	8.5 (9)	2.68 (1)

3.4. X-ray absorption spectroscopy (XANES and EXAFS)

3.4.1. Extended X-ray absorption fine structure (EXAFS)

Figs. 7 and 8 show k^2-weighted EXAFS spectra at the Pt L$_3$-edge and the corresponding radial distribution function for each sample. The intensity at a given distance is proportional to the number of scatterers located at that distance from an absorber atom. Before H$_2$ treatment, samples show significant Pt–O coordination, but reduced samples give radial structures consistent with predominant Pt–Pt coordination, except for minor Pt–O contributions, especially in the 1.6 wt.% Pt/Al$_2$O$_3$ sample.

XANES spectra were acquired and analyzed to determine the origin of these oxygen contributions. Fig. 9a shows L$_3$ XANES spectra for bulk PtO$_2$ and a foil of Pt. Electron transfer from Pt to O atoms in PtO$_2$ leads to a stronger white line in PtO$_2$ compared with the foil. Fig. 9b shows L$_3$ XANES spectra for a foil of Pt and for the 1.6 wt.% Pt/Al$_2$O$_3$ sample before and after exposure to air. Exposure to air leads to a more intense white line, as a result of the oxidation of Pt cluster surfaces. Reduced samples, in contrast, show a less intense white line than bulk Pt, indicating that they remain metallic during the acquisition of the spectra; thus, we conclude that Pt–O coordination in reduced samples reflect contact of some Pt atoms with O-atoms on the support surface.

EXAFS spectra were analyzed using standard procedures [37]. Theoretical standards were generated using multiple scattering simulations in FEFF7 [24]. Table 1 and Fig. 10 show the results corresponding to the Pt–Pt shell of the EXAFS fitted functions. Pt atoms in supported catalysts show average coordination numbers smaller than in bulk Pt ($N = 12$), as well as smaller Pt–Pt distances (2.67 Å versus 2.77 Å). The same observed Pt–Pt distance contraction in supported nanoclusters respect to the bulk (3.6%) has been detected and
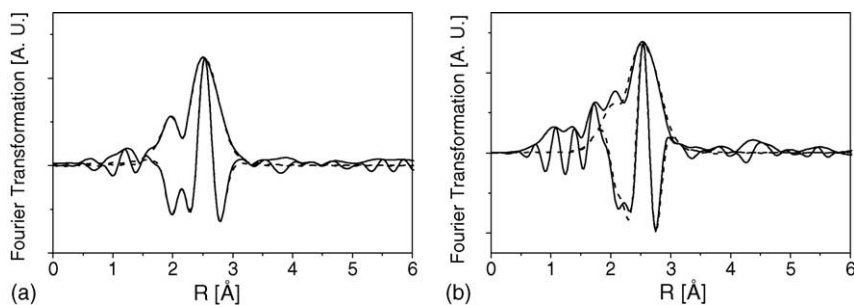

Fig. 9. L$_3$ XANES spectra of (a) PtO$_2$ and bulk Pt (b) bulk Pt, 1.6 wt.% Pt/Al$_2$O$_3$ sample measured in situ and 1.6 wt.% Pt/Al$_2$O$_3$ sample measured after exposure to air.

Fig. 10. Fourier transforms of EXAFS data of samples 0.8 wt.% Pt/Al$_2$O$_3$ (a) and 1.6 wt.% Pt/Al$_2$O$_3$ (b). Solid line shows amplitude and imaginary part of the Fourier transforms. Dashed lines show the corresponding Fourier transforms of the fitted functions.
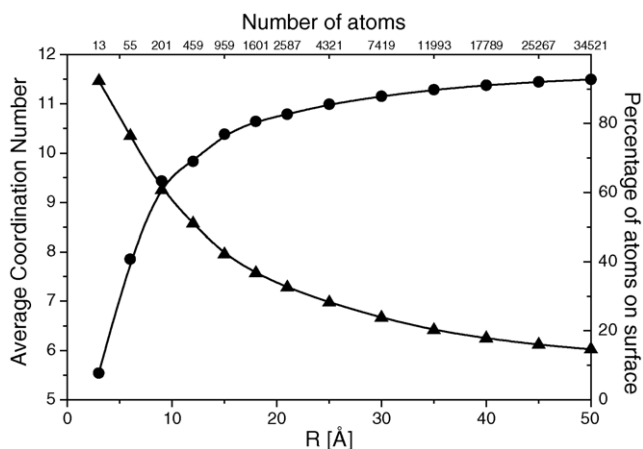

Fig. 11. Average coordination number as a function of spherical particles as a function of the radius size or number of atoms (circles) and percentage of surface atoms in function of size (triangles).

calculated previously as a result of changes in temperature [38–40] or hydrogen chemisorption [38,41,42] and also predicted from changes in size of metal clusters [43].

The size of these clusters was estimated from average coordination numbers obtained from EXAFS fits and from calculated average coordination numbers for spherical fcc Pt clusters of varying size (Fig. 11). This analysis led to average diameters of 1.2 ± 0.2 and 1.5 ± 0.3 nm for 0.8 wt.% Pt/Al$_2$O$_3$ and 1.6 wt.% Pt/Al$_2$O$_3$, respectively, in reasonable

agreement with the conclusion from scattering data. These values provide lower limits estimates of cluster size, because of the assumption of spherical clusters of uniform size. Deviations from spherical shape, would lead to higher surface-to-volume ratios for a given number of atoms in the cluster and to size estimates smaller than those obtained from dispersion measurements.

3.5. X-ray absorption near edge spectroscopy (XANES)

XANES data were acquired at the Pt L$_2$ and L$_3$ absorption edges for 0.8 wt.% Pt/Al$_2$O$_3$ and 1.6 wt.% Pt/Al$_2$O$_3$ in N$_2$ after evacuating at 773 K the H$_2$ used to reduce samples in situ. Normalized L$_{2,3}$ XANES spectra for each sample and for a Pt foil are shown in Fig. 12. The spectra for the two samples are similar to each other, but differ significantly from those for Pt foil. The L$_2$ and L$_3$ absorption edge energies, however, are very similar for Pt/Al$_2$O$_3$ samples and Pt foil indicating the presence of metallic Pt atoms in all samples. Difference spectra were obtained by subtracting the Pt foil reference spectrum from that of each sample at the two L-edges. L$_2$ difference spectra (Fig. 13a) contain a weak negative feature near the edge and a strong positive feature at 8 eV above the edge, while L$_3$ difference spectra (Fig. 13b) give a stronger negative feature above the edge and a similar positive one at 8 eV. Similar results for reduced Pt/SiO$_2$ samples have been reported previously [27,41]. The strong negative feature arises
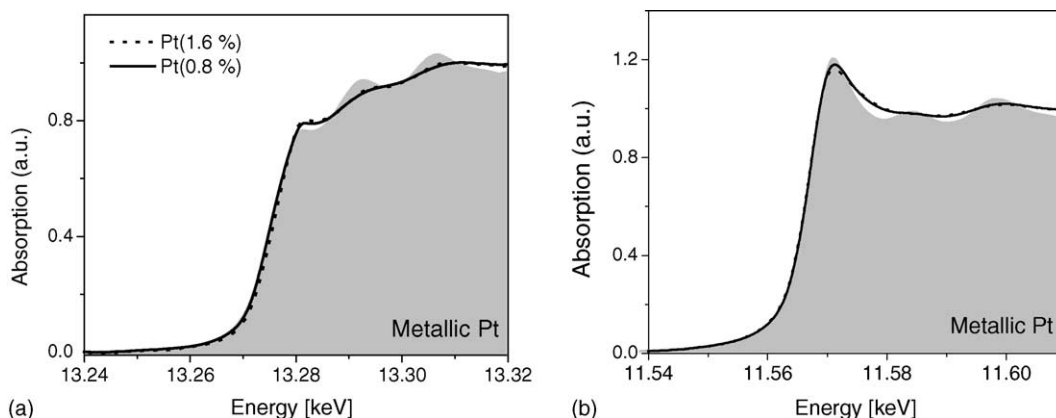

Fig. 12. XANES spectra of the L$_2$ (a) and L$_3$ (b) edges of Pt/Al$_2$O$_3$ samples (black lines) and bulk Pt (gray shadow).
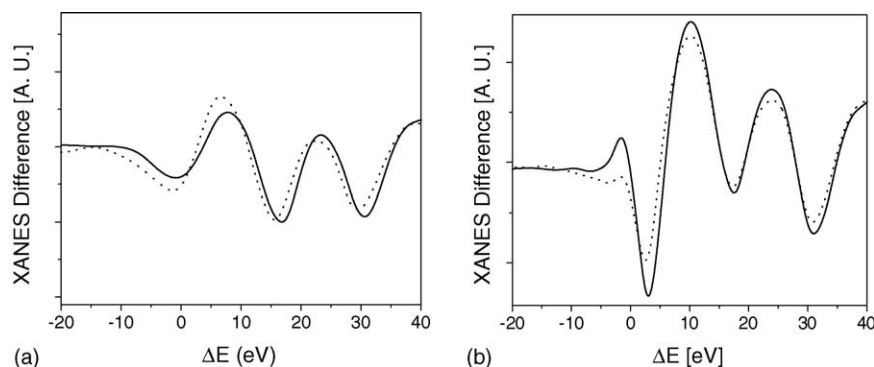
Fig. 13. Difference spectra between the absorption L_2 (a) and L_3 (b) edges of 0.8 wt.% Pt/Al_2O_3 (solid lines) and 1.6 wt.% Pt/Al_2O_3 (dotted lines) samples and bulk Pt.

from a less intense white line in supported samples than in Pt foil, indicative of a higher 5d electron density in supported samples [23,24]. Ramaker et al. have proposed that the peaks at 8 eV can be attributed to Pt–H EXAFS [44]. The spectral features in the 15–40 eV region reflect the structure near Pt atoms and not their electronic environment or structure. The negative feature at 15 eV, present in both L_2 and L_3 difference spectra resembles in position the maximum of the first oscillation beyond the L_3 white line of Pt foil. Hence, this negative feature can be attributed to a decrease in the coordination number of Pt atoms in the clusters relative to the environment in bulk Pt [45].

The number of d-band vacancies in Pt clusters was estimated using a modified version of previously reported methods [26]. The absorption edges of each sample and of Pt foil were aligned and their differences in the neighborhood of the white line were obtained from integrated intensities. The fractional change in the total number of empty states in the d-band (f_d) was estimated from Eq. (4) and the results are shown in Table 2. Pt atoms in both samples show fewer 5d vacancies than bulk Pt. More significantly, these effects arise predominately from changes in electron density for surface atoms, which differ significantly in environment from those in the bulk. The contributions from surface atoms to the observed change in 5d electronic density were estimated from the values of Fig. 10 and the assumption of quasi-spherical clusters and the results are shown in Table 2. These contributions are similar for the two samples and they indicate that differences in 5d electron density between surface and bulk atoms are much greater than any differences in surface atom electron density resulting from changes in cluster size. Consequently, differences in the 5d electronic density of Pt

surface atoms between these two samples cannot be detected by these experiments, even though the relative amount of surface atoms differs by ~15% between them. Although these results would suggest that the different catalytic properties of the catalysts should be attributed to nanoclusters structure (size and shape) mainly, we cannot unequivocally exclude the underlying relation between structure and electronics in this case. This ambiguity reflects the ensemble-averaging nature of the XANES experiments. The total XANES signal arises from both bulk and surface atoms and only a small percentage of the last ones would have differences between the two samples. These differences in electronic density coming from active surface Pt atoms are attenuated in the total XANES signal so that they are of the order of the experimental error in our determinations. Having this in mind, we cannot discard that the changes observed in the nanoclusters structure are associated with changes in the electronic structure from coordinative unsaturated surface Pt atoms.

4. Conclusions

Four complementary methods (H_2 chemisorption, HRTEM, SAXS and EXAFS) were used to determine the sizes of supported Pt clusters in catalysts used for reforming of methane to produce synthesis gas. These techniques emphasize different components of the Pt cluster size distribution. EXAFS and SAXS detect smaller clusters (1.2–1.5 nm range) than HRTEM methods (2–3 nm range). The results are in reasonable qualitative agreement, especially in light of the assumption of quasi-spherical clusters required to transform scattering, absorption, and microscopy results into estimates of cluster size.

XANES data indicate that the density of d-electrons is greater on surface than bulk Pt atoms, but changes in electronic properties from XANES spectra were not detected within the range of Pt cluster size examined in this study. Thus, the marked catalytic consequences of Pt clusters size reported here appear to reflect changes in structure and local coordination of surface Pt atoms, which vary gradually with changes in cluster size.

Table 2
Intensity of Pt L_2 and L_3 X-ray absorption edges on Pt/SiO_2 and $PtSn/SiO_2$ in Ar and in H_2, their corresponding fractional change in the total number of unfilled states in the d-band compared to the platinum foil (f_d) and the contribution per atom in surface to this change (f_s)

Sample	ΔA_2 (eV)	ΔA_3 (eV)	f_d	f_s ($\times 10^{-3}$)
0.8 wt.% Pt/Al_2O_3	−0.042	−0.177	−0.027	−3.4
1.6 wt.% Pt/Al_2O_3	−0.046	−0.151	−0.023	−3.5

Acknowledgements

References

[1] B. Jenewein, M. Fuchs, K. Hayek, Surf. Sci. 532 (2003) 364.
[2] M. Agnelli, C. Mirodatos, J. Catal. 192 (2000) 204.
[3] M.C.J. Bradford, M.A. Vannice, Appl. Catal. A 142 (1996) 97.
[4] J.R. Rostrup-Nielsen, J.H. Bak Hansen, J. Catal. 144 (1993) 38.
[5] Z.L. Zhang, V.A. Tsipouriari, A.M. Efstathiou, X.E. Verykios, J. Catal. 158 (1996) 51.
[6] S. Arrii, F. Morfin, A.J. Renouprez, J.L. Rousset, J. Am. Chem. Soc. 126 (2004) 1199.
[7] M. Boudart, Adv. Catal. 20 (1969) 153.
[8] J. Wei, E. Iglesia, J. Catal. 225 (2004) 116.
[9] J. Wei, E. Iglesia, J. Phys. Chem. B 108 (2004) 7253.
[10] J. Wei, E. Iglesia, Angew. Chem. Int. Ed. 43 (2004) 3685.
[11] J. Wei, E. Iglesia, J. Phys. Chem. B 108 (2004) 4094.
[12] D.F. Johnson, W.H. Weinberg, J. Chem. Phys. 101 (1994) 6289.
[13] J.F. Weaver, M.A. Krzyzowski, R.J. Madix, Surf. Sci. 391 (1997) 150.
[14] P.D. Szuromi, J.R. Engstrom, W.H. Weinberg, J. Phys. Chem. 89 (1985) 2497.
[15] O. Kratky, O. Glatter, Small-Angle X-ray Scattering, Academic Press, London, 1982.
[16] A. Guinier, G. Fournet, Small-Angle Scattering of X-rays, Wiley, 1955.
[17] M. Boudart, G. Djega-Mariadassou, The Kinetics of Heterogeneous Catalytic Reactions, Princeton University Press, Princeton, NJ, 1984.
[18] G. Kellerman, F. Vicentin, E. Tamura, M. Rocha, H. Tolentino, A. Barbosa, A. Craievich, I. Torriani, J. Appl. Crystallogr. 30 (1997) 880.
[19] W. Ruland, J. Appl. Cryst. 4 (1971) 70.
[20] T. Ressler, S.L. Brock, J. Wong, S.L. Suib, J. Phys. Chem. B 103 (1999) 6407.
[21] T. Ressler, J. Synch. Rad. 5 (1998) 118.
[22] S.I. Zabinsky, J.J. Rehr, A. Ankudinov, R.C. Albers, M.J. Eller, Phys. Rev. B 52 (1995) 2995.
[23] F.W. Lytle, P.S.P. Wei, R.B. Greegor, G.H. Via, J.H. Sinfelt, J. Chem. Phys. 70 (1979) 4849.
[24] F.W. Lytle, J. Catal. 43 (1976) 376.
[25] G. Meitzner, G.H. Via, F.W. Lytle, J.H. Sinfelt, J. Phys. Chem. 96 (1992) 4960.
[26] A.N. Mansour, J.W. Cook Jr., D.E. Sayers, J. Phys. Chem. 88 (1984) 2330.
[27] S.N. Reifsnyder, M.M. Otten, D.E. Sayers, H.H. Lamb, J. Phys. Chem. B 101 (1997) 4972.
[28] M. Brown, R.E. Peierls, E.A. Stern, Phys. Rev. B 15 (1977) 738.
[29] W.H. McMaster, N. Kerr Del Grande, J.H. Hubell, Compilation of X-ray Cross Sections, National Technical Information Service, Springfield, VA.
[30] R. Pitchai, K. Klier, Catal. Rev.-Sci. Eng. 28 (1986) 13.
[31] D.F. Johnson, H. Weinberg, Science 261 (1993) 5117.
[32] D.F. Johnson, H. Weinberg, J. Chem. Phys. 103 (1995) 5833.
[33] R.M. Watwe, H.S. Bengaard, J.R. Rosrrup-Nielsen, J.A. Dumesic, J.K. Norskov, J. Catal. 189 (2000) 16.
[34] M. Schneider, D.G. Duff, T. Mallat, M. Wildberger, A. Baiker, J. Catal. 147 (1994) 500.
[35] A. Renouprez, C. Hoan-Van, P.A. Compagnon, J. Catal. 34 (1974) 411.
[36] H.G. Haubold, X.H. Wang, G. Goerick, W. Schilling, J. Appl. Cryst. 30 (1997) 653.
[37] D.C. Koningsberger, B.L. Mojet, G.E. van Dorssen, D.E. Ramaker, Top. Catal. 10 (2000) 143.
[38] M.K. Oudenhuijzen, P.J. Kooyman, B. Tappel, J.A. van Bokhoven, D.C. Koninsberger, J. Catal. 205 (2002) 135.
[39] S. Schneider, D. Bazin, F. Garin, G. Maire, M. Capelle, G. Meunier, R. Noroit, Appl. Catal. A 189 (1999) 139.
[40] N.S. Guyot-Sionnest, F. Villain, D. Bazin, H. Dexpert, F. Le Peltier, J. Lynch, J.P. Bournonville, Catal. Lett. 8 (1991) 283.
[41] G. Santori, M. Casella, O. Ferretti, J.M. Ramallo-López, L. Giovanetti, F.G. Requejo, J. Phys. Chem. B 107 (2003) 11441.
[42] B. Moraweck, A.J. Renouprez, Surf. Sci. 10 (1981) 635.
[43] C. Monnet, G. Treglia, B. Legrand, Surf. Sci. 383 (1997) 719.
[44] D.E. Ramaker, B.L. Mojet, M.T. Garriga Oostenbrink, J.T. Miller, D.C. Koningsberger, Phys. Chem. Chem. Phys. 1 (1999) 2293.
[45] M.G. Samant, M. Boudart, J. Phys. Chem. 95 (1991) 4070.